JACS
JOURNAL OF THE AMERICAN CHEMICAL SOCIETY
Article
pubs.acs.org/JACS

Chirality Driven Metallic versus Semiconducting Behavior in a Complete Series of Radical Cation Salts Based on Dimethyl-Ethylenedithio-Tetrathiafulvalene (DM-EDT-TTF)

Flavia Pop,[†] Pascale Auban-Senzier,[‡] Arkadiusz Frąckowiak,[§] Krzysztof Ptaszyński,[§] Iwona Olejniczak,[§] John D. Wallis,[∥] Enric Canadell,[⊥] and Narcis Avarvari*[,†]

[†]Laboratoire MOLTECH-Anjou, UMR 6200, UFR Sciences, Université d'Angers, CNRS, Bâtiment K, 2 Bd. Lavoisier, 49045 Angers, France

[‡]Laboratoire de Physique des Solides, UMR 8502, Université Paris-Sud, Bâtiment 510, 91405 Orsay, France

[§]Institute of Molecular Physics, Polish Academy of Sciences, Smoluchowskiego 17, 60-179 Poznan, Poland

[∥]School of Science and Technology, Nottingham Trent University, Clifton Lane, Nottingham, NG11 8NS, United Kingdom

[⊥]Institut de Ciència de Materials de Barcelona (CSIC), Campus de la UAB, E-08193 Bellaterra, Spain

Supporting Information

ABSTRACT: Enantiopure (*S*,*S*) and (*R*,*R*) dimethyl-ethylenedithio-tetrathiafulvalene (DM-EDT-TTF) **1** donors are synthesized by cross coupling followed by decarboxylation reactions. In the solid state the methyl groups are arranged in axial positions within sofa-type conformation for the six-membered rings. Crystalline radical cation salts formulated as $[(S,S)\text{-}\mathbf{1}]_2PF_6$, $[(R,R)\text{-}\mathbf{1}]_2PF_6$, and $[(rac)\text{-}\mathbf{1}]_2PF_6$ are obtained by electrocrystallization. When the experiment is conducted with enantioenriched mixtures both enantiopure and racemic phases are obtained. The monoclinic enantiopure salts, containing four independent donors in the unit cell, show semiconducting behavior supported by band structure calculations of extended Hückel type. The racemic salt contains only one independent donor in the mixed valence oxidation state +0.5. Under ambient pressure the racemic material is metallic down to 120 K, while an applied pressure of 11.5 kbar completely suppresses the metal−insulator transition. Band structure calculations yield an open Fermi surface, typical for a pseudo-one-dimensional metal, with unperfected nesting, thus ruling out the possibility of charge or spin density modulations to be at the origin of the transition. Raman spectroscopy measurements, in agreement with structural analysis at 100 K, show no indication of low-temperature charge ordering in the racemic material at ambient pressure, thus suggesting Mott-type charge localization for the observed metal−insulator transition.

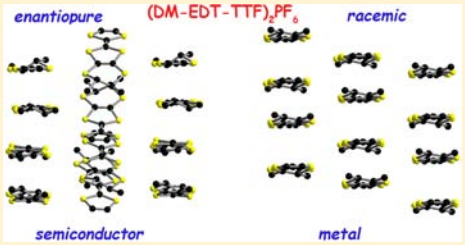

INTRODUCTION

The research activity in the field of chiral tetrathiafulvalenes (TTF),[1] as part of the more general family of multifunctional molecular materials,[2] has been continuously developing especially in the past decade, although the first example of an enantiopure TTF derivative, i.e., the (*S*,*S*,*S*,*S*) enantiomer of tetramethyl-bis(ethylenedithio)-tetrathiafulvalene (TM-BEDT-TTF), has been described back in the middle of the 1980s by Dunitz and Wallis.[3] The increasing interest in these chiral precursors and the materials derived thereof is currently motivated by several features: (i) possible redox modulation of the chiroptical properties;[4] (ii) detection of an electrical magnetochiral-anisotropy effect, solely observed so far in molecular materials in the case of chiral carbon nanotubes;[5] (iii) influence of the chirality on the conducting properties through the modulation of the structural disorder in the solid state, as demonstrated within complete series of conducting salts based on ethylenedithio-tetrathiafulvalene-oxazoline (EDT-TTF-Ox) donors.[6] Accordingly, although similar crystal structures were observed for enantiopure and racemic compounds, the conductivity was 1 order of magnitude lower for the racemic than for the enantiopure salts formulated as $(EDT\text{-}TTF\text{-}Ox)_2(XF_6)$ (X = As, P), as a consequence of the structural disorder present in the racemic form. In order to address the several challenges related to the influence and role of chirality when present in TTF precursors and materials derived thereof, TTF derivatives with different types of chirality have been described,[1] besides the EDT-TTF-Ox already mentioned. For example, TTF-bis(oxazolines),[7] bis(pyrrolo)-TTFs,[8] C_3 symmetric tris(TTF) affording supramolecular helical aggregates,[9] TTF-sulfoxides,[10] TTF-binaphthyls,[11] or TTF-allenes[4] have been reported. However, in spite of peculiar solid-state architectures, self-assembly behavior, or chiroptical properties, none of these different precursors provided so far conducting salts. Furthemore, although methylated BEDT-TTF derivatives, such as tetramethyl-BEDT-TTF (TM-BEDT-TTF)[3,12] and dimethyl-BEDT-TTF (DM-BEDT-TTF)[12,13] or

Received: August 16, 2013
Published: October 22, 2013

dimethyl-EDT-TTF (DM-EDT-TTF)[14] (Chart 1), are known for more than 25 years, no complete series of conducting salts

Chart 1

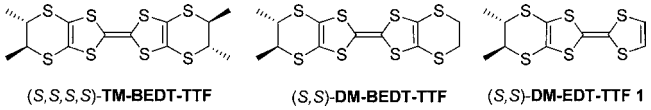

including both enantiomeric and racemic forms has been described so far, except for a very recent series of 1:1 semiconducting salts of TM-BEDT-TTF with the I_3^- anion.[15] In the latter, the structural disorder induces once again a much lower conductivity for the racemic salt than for the enantiopure ones. Moreover, while a few chiral conducting salts have been reported with either (*S*) or (*R*) enantiomers of TM-BEDT-TTF[16] or DM-BEDT-TTF[17] and various anions, including a recent example of a chiral ferromagnetic metal,[18] there is no mention of any chiral conducting phase based on the DM-EDT-TTF donor **1**.[19] We describe herein the synthesis and solid-state structures of enantiopure (*S*,*S*) and (*R*,*R*)-**1**, together with the first complete series of conducting mixed valence salts and their physical properties, showing massive differences between the racemic and enantiopure forms. Raman spectroscopy investigations on the possibility of the occurrence of charge ordering at low temperature are also presented.

RESULTS AND DISCUSSION

Synthesis and Characterization of the Neutral Donor. The synthesis of DM-EDT-TTF was previously very briefly mentioned,[14] though without any stereochemical related discussion nor any analytical characterization. Now, the preparation of both enantiomers (*S*,*S*)-**1** and (*R*,*R*)-**1** is thoroughly described, being conducted by phosphite-mediated heterocoupling between one of the enantiopure dithiolethiones (*S*,*S*)-**2** and (*R*,*R*)-**2**, obtained by a slightly modified literature procedure,[12] and the dithiolone diester **3** (see SI for full experimental details), followed by a double decarboxylation of the resultant intermediate **4** (Scheme 1).

Scheme 1. Synthesis of Enantiopure DM-EDT-TTF 1

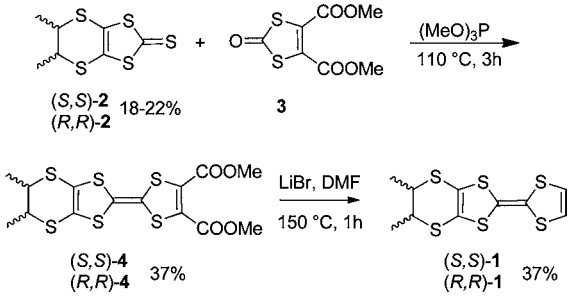

Cyclic voltammetry measurements show the classical reversible two single electron oxidation processes into radical cation and dication species at $\Delta E_{1/2}$ = +0.44 and 0.78 V vs SCE, respectively (Figure S1).

Single crystals for both enantiomers could be grown by slow evaporation from a $Et_2O-CH_2Cl_2$ solvent mixture. The X-ray analysis shows that they crystallize in the orthorhombic noncentrosymmetric space group $P2_12_12_1$ with one independent molecule in the unit cell. The dithiin six-membered ring shows a sofa-type conformation with axial orientation of the methyl substituents (Figure 1), as in the case of DM-BEDT-TTF,[12] and boat-like conformation of the TTF unit, with distortions of 18° and 9.5° about the S3···S4 and S1···S2 axis, respectively. Note that the dithiin ring can in principle adopt half-chair or sofa conformations when the outer sp^3 C7 and C8 atoms lie above and below the S5C5C6S6 mean plane or a boat conformation when they are on the same side of this mean plane.[12] The difference between half-chair and sofa relies on the magnitude of the dihedral angles τ_1 and τ_2, corresponding respectively to the C5−C6−S6-C7 and C6−C5−S5-C8 angles. When both of them exceed 7.5° the conformation is defined as half-chair, which is equivalent with a strong distortion, while a sofa conformation is characterized by at least one of the angles smaller than 7.5°.

Recent theoretical calculations in the case of TM-BEDT-TTF show that the axial conformer is more stable than the equatorial one, while in the solid state only the latter was observed, probably because of the more favorable packing.[15] However, the energy difference amounts to 1.25 kcal·mol^{-1} only, indicating that both conformers are in equilibrium in solution, which is very likely the case also with DM-EDT-TTF **1**. Bond lengths, especially the central C3═C4 and internal C−S bonds, have typical values for neutral donors (Table 1).

Table 1. Selected Bond Distances for Neutral (*S*,*S*)-1 and (*R*,*R*)-1

bond lengths (Å)	
(*R*,*R*)-**1**	(*R*,*R*)-**1**
C3═C4 1.332(5)	C3═C4 1.333(8)
S4−C4 1.759(5)	S4−C4 1.737(7)
S3−C4 1.748(5)	S3−C4 1.753(7)
S2−C3 1.762(6)	S2−C3 1.796(8)
S1−C3 1.771(6)	S1−C3 1.760(8)

The packing of the molecules show formation of zigzag chains along the *b* direction, with quite long S···S intermolecular distances of 3.81−3.83 Å, while in the *ac* plane the donors arrange in a perpendicular manner, without any short S···S intermolecular contact (see Figures S2 and S3). This type of packing is completely different to the one described for the unsubstituted EDT-TTF donor where

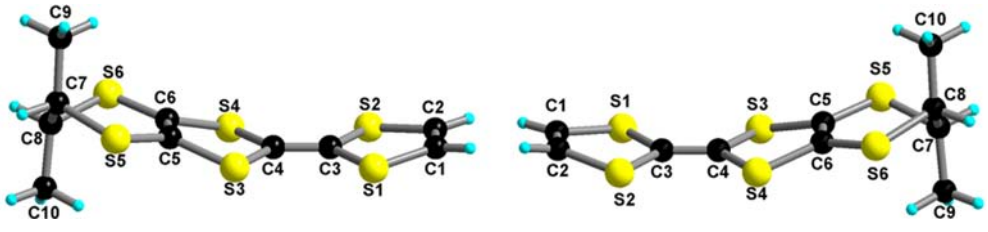

Figure 1. Molecular structure of (*S*,*S*)-**1** (left) and (*R*,*R*)-**1** (right) together with atom numbering scheme.

dx.doi.org/10.1021/ja408350r | J. Am. Chem. Soc. 2013, 135, 17176−17186

formation of orthogonal dyads is observed,[20] thus demonstrating the huge influence of the two additional methyl groups.

Synthesis and Characterization of the Radical Cation Salts $(1)_2PF_6$. Electrocrystallization experiments of enantiopure or racemic **1**, the latter being obtained by mixing equimolar amounts of pure enantiomers, in chloroform solutions in the presence of $[(n\text{-Bu})_4N]PF_6$ afforded mixed valence salts formulated as $(1)_2PF_6$. Having in mind that trace amounts of an impurity can alter the course of a chiral process,[21] we have employed exactly the same experimental conditions in the three cases. In spite of identical stoichiometry, the structures of the racemic and enantiopure forms are completely different. The only common structural feature for both enantiopure $(1)_2PF_6$ and $[(rac)\text{-}1]_2PF_6$ salts is the equatorial arrangement adopted by the Me substituents, very likely as a means to maximize the intermolecular interactions between the oxidized species, within a sofa conformation for the dithiin ring. The enantiopure (*S*,*S*) and $[(R,R)\text{-}1]_2PF_6$ salts are isostructural and crystallize in the chiral space group $P2_1$ of the monoclinic system, with four independent donor molecules **A**−**D** alternating along *b* in a **CABD** sequence (Figure 2 for the (*S*,*S*) enantiomer), and two independent PF_6 anions in the asymmetric unit. The donors **A** and **B** show planar geometries, while **C** and **D** are clearly bent in a boat conformation, with dihedral angles of 20.3° (S3C···S4C) and 12.5° (S1C···S2C) for **C** and 18.2° (S3D···S4D) and 9.2° (S1D···S2D) for **D**.

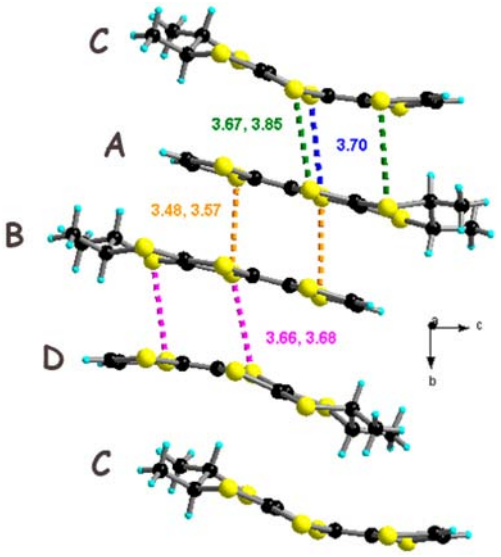

Figure 2. Sequence of donors along *b* in the structure of $[(S,S)\text{-}1]_2PF_6$. Short intrastack S···S contacts (some of them are highlighted) (Å): S3C···S4A 3.67, S4C···S3A 3.70, S1C···S6A 3.85, S1A···S3B 3.48, S2A···S4B 3.60, S3A···S1B 3.57, S4A···S2B 3.53, S5B···S2D 3.68, S3B···S4D 3.66, S4B···S3D 3.81.

The analysis of the central C═C and internal C−S bond lengths (Table 2), showing longer C═C and shorter C−S bonds for **A** and **B** when compared to **C**, **D** and the neutral donor (*vide supra*), clearly indicates that the molecules **A** and **B** bear a more positive charge than **C** and **D**, in agreement with their respective planar or bent shapes.

The shortest intrastack S···S contacts, amounting at 3.48−3.60 Å, are established between donors **A** and **B**, while longer distances of 3.66−3.85 Å are observed between **A** and **C** or **B** and **D**. Note that the shortest S···S contacts between **C** and **D** exceed 4.2 Å, a much longer value than the van der Waals sum of ∼3.70 Å for two S atoms. It is thus expected that the strongest interaction along the stack takes place between **A** and **B**. Furthermore, the donors are arranged in parallel columns alternating along *a*, with rather long interstack S···S distances of 4 Å for the shortest ones between donors belonging to neighboring columns which are inclined by 32° with respect each other. There is no classical organic−inorganic segregation in the packing, since each PF_6 anion is surrounded by donor molecules interacting through a complex set of H_{vinyl}···F and H_{Me}···F hydrogen bonds of 2.41−2.81 and 2.44−2.68 Å, respectively (Figures 3 and S4).

Table 2. Selected Bond Distances for $[(S,S)\text{-}1]_2PF_6$ and $[(R,R)\text{-}1]_2PF_6$

	bond lengths (Å)	
	$(S,S)\text{-}(1)_2PF_6$	$(R,R)\text{-}(1)_2PF_6$
A	C3A-C4A 1.385(8)	C3A-C4A 1.390(7)
	S4A-C4A 1.731(5)	S4A-C4A 1.727(5)
	S3A-C4A 1.721(5)	S3A-C4A 1.719(5)
	S2A-C3A 1.728(6)	S2A-C3A 1.720(5)
	S1A-C3A 1.710(5)	S1A-C3A 1.722(5)
B	C3B−C4B 1.396(8)	C3B−C4B 1.387(7)
	S4B−C4B 1.727(6)	S4B−C4B 1.723(4)
	S3B−C4B 1.718(5)	S3B−C4B 1.724(5)
	S2B−C3B 1.729(5)	S2B−C3B 1.720(5)
	S1B−C3B 1.717(6)	S1B−C3B 1.725(5)
C	C3C−C4C 1.364(9)	C3C−C4C 1.339(7)
	S4C−C4C 1.761(6)	S4C−C4C 1.753(5)
	S3C−C4C 1.745(6)	S3C−C4C 1.766(5)
	S2C−C3C 1.749(6)	S2C−C3C 1.762(5)
	S1C−C3C 1.750(6)	S1C−C3C 1.750(5)
D	C3D-C4D 1.321(9)	C3D-C4D 1.353(8)
	S4D-C4D 1.767(5)	S4D-C4D 1.760(5)
	S3D-C4D 1.762(6)	S3D-C4D 1.750(5)
	S2D-C3D 1.761(6)	S2D-C3D 1.751(5)
	S1D-C3D 1.770(6)	S1D-C3D 1.755(6)

The structure of the racemic salt $(1)_2PF_6$ has been determined both at room temperature and 100 K in order to verify the possible occurrence of a structural phase transition (*vide infra*). However, excepting the usual thermal contraction of the cell parameters, the structure does not change. The compound crystallizes in the triclinic system with centrosymmetric space group *P*-1. In both cases one independent molecule of donor, in a general position, and half a molecule of anion, located on the inversion center, are contained in the asymmetric unit. The other enantiomer together with the other half of anion are generated through the inversion center, therefore the mean charge on each TTF is +0.5. Accordingly, the TTF unit is planar (Figure S5), and the central C═C and internal C−S bond lengths (Table 3) are in agreement with a mixed valence oxidation state for TTF. Note that similar values for the bond lengths are measured for the low-temperature structure.

The donors stack in parallel columns, an arrangement reminiscent of the β structural type,[22] with intrastack and interstack S···S contacts of 3.62−3.67 Å and 3.46−3.70 Å, respectively (Figure 4).

Once again all six fluorine atoms of the anion are involved in short H_{vinyl}···F and H_{Me}···F contacts amounting at 2.48−2.66 Å and 2.64−2.70 Å, respectively (Figure 5).

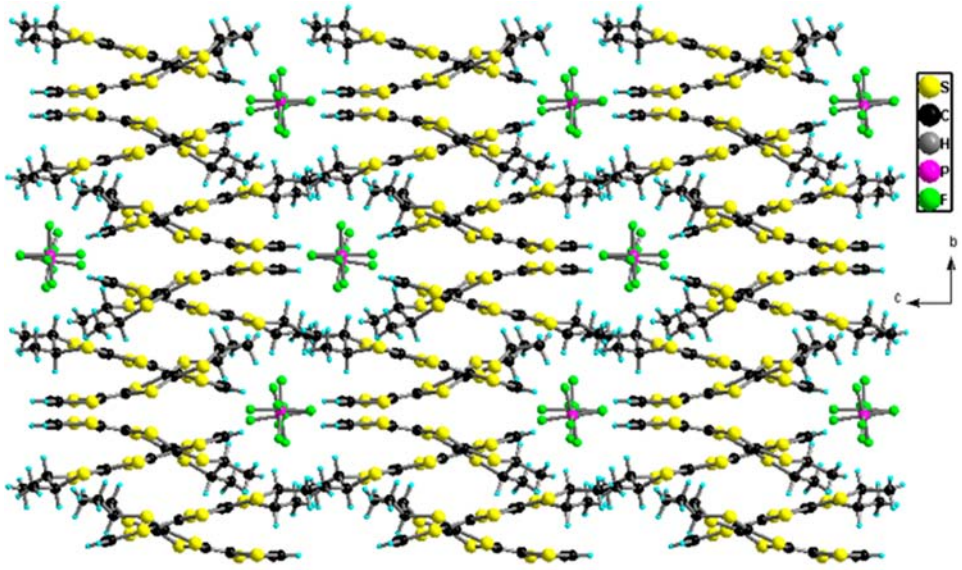

Figure 3. Packing diagram of $[(S,S)\text{-}\mathbf{1}]_2PF_6$ in the *bc* plane.

Table 3. Selected Bond Distances for $[(rac)\text{-}\mathbf{1}]_2PF_6$

bond length (Å)	
RT	100 K
C3−C4 1.372(5)	C3−C4 1.374(5)
S4−C4 1.739(4)	S4−C4 1.745(4)
S3−C4 1.743(4)	S3−C4 1.738(4)
S2−C3 1.739(4)	S2−C3 1.744(4)
S1−C3 1.740(4)	S1−C3 1.746(4)

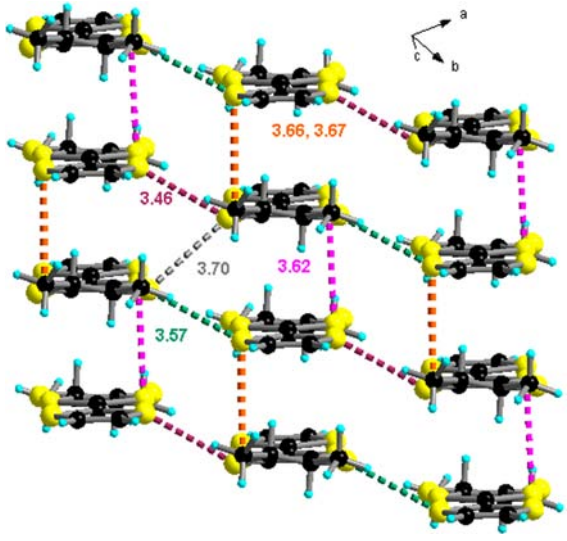

Figure 4. Packing diagram of $[(rac)\text{-}\mathbf{1}]_2PF_6$ with an emphasis on the S···S short contacts. PF_6 anions have been omitted.

Interestingly, when a mixture of **1** with 50% ee in (*S*,*S*) enantiomer was electrocrystallized in the same conditions, in order to check the formation of enantioenriched phases, two types of crystals were observed, corresponding to the enantiopure (*S*,*S*) phase and the racemic one. Very likely, since the structural features of the two phases are quite different, the donor prefers to crystallize in either both structural types and not in an intermediate enantioenriched polymorph.

Conducting Properties and Band Structure Calculations. When considering the completely different solid-state structures of the enantiopure salts compared to the racemic one, significant differences in the conducting properties are expected to occur. In the literature so far, the comparison between the conducting properties of racemic and enantiopure TTF-based radical cation salts shows that the enantiopure phases are more conducting than the racemic one because of the structural disorder present in the latter.[6b,c,15] However, in all these examples the structures of the enantiopure and racemic salts were identical excepting the disorder. A similar behavior was observed when the achiral BEDT-TTF donor was electrocrystallized into conducting mixed valence salts $[BEDT\text{-}TTF]_4[(NH_4)Fe(Ox)_3]$ (Ox = oxalate) in the presence of either enantiopure or racemic *sec*-phenethyl alcohol as electrocrystallization solvent.[23] The salt containing the racemic solvent, which crystallized with an occupational disorder, shows a more abrupt metal−insulator (MI) transition. In the present series of salts, however, the structures are very different, with the presence of charge-rich and -poor donors in the case of the enantiopure salts and strong dimerization within the stacks. Single crystal conductivity measurements show similar semiconducting behaviors for $[(S,S)\text{-}\mathbf{1}]_2PF_6$ and $[(R,R)\text{-}\mathbf{1}]_2PF_6$ salts, with a low conductivity value at room temperature $\sigma_{RT} \approx 10^{-5}$ $S{\cdot}cm^{-1}$ and an activation energy, $E_a \approx 3900$ K, deduced from a fit of the data to a law of the type $\sigma = \sigma_0 \exp(E_a/kT)$ (Figure 6).

The calculated band structures for the (*S*,*S*) (Figure 7) and (*R*,*R*) (Figure S9) are, as expected, identical, and therefore in the following only the former will be discussed. The four independent molecules of donors are labeled **A**−**D** according to their central C═C bond (see Table 2), and, therefore, **A** and **B** are the "planar" donors, while **C** and **D** are the "strongly bent" donors.

Since the repeat unit of the donor layers contains eight donors, the band structure of Figure 7 contains eight HOMO-based bands. As the average donor charge is +1/2 these bands must be filled with 12 electrons. Consequently, there is a band gap separating the upper pair of empty bands from the filled ones, and thus these salts must have activated conductivity, in agreement with the single crystal resistivity measurements (see Figure 6). The upper pair of bands is almost exclusively made

dx.doi.org/10.1021/ja408350r | J. Am. Chem. Soc. 2013, 135, 17176−17186

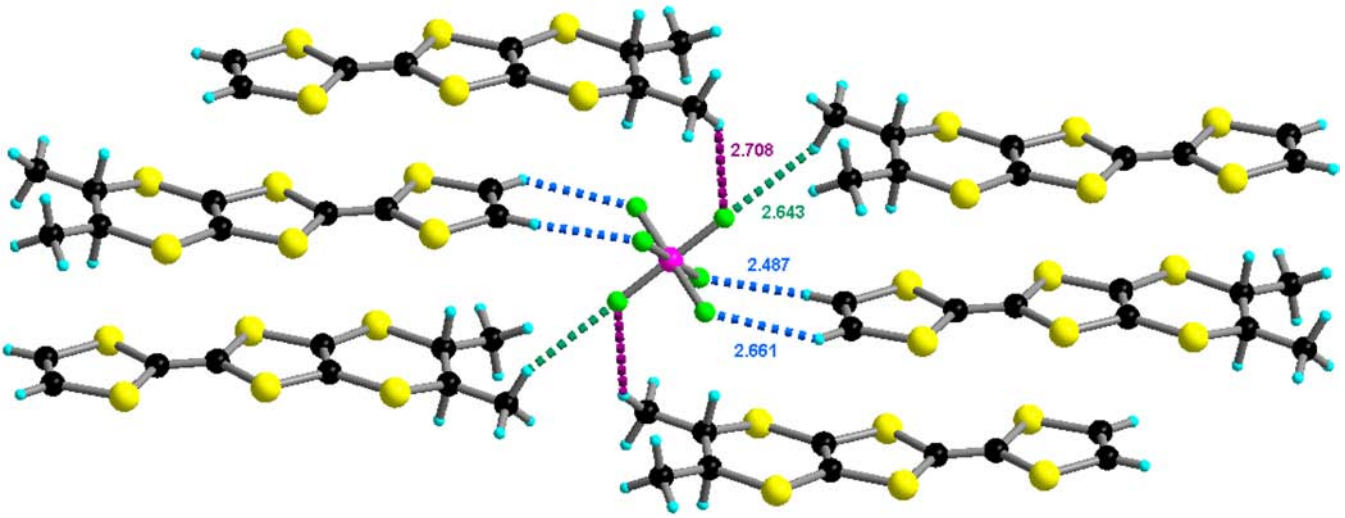

Figure 5. CH···F short contacts in the structure of $[(rac)\text{-}\mathbf{1}]_2PF_6$.

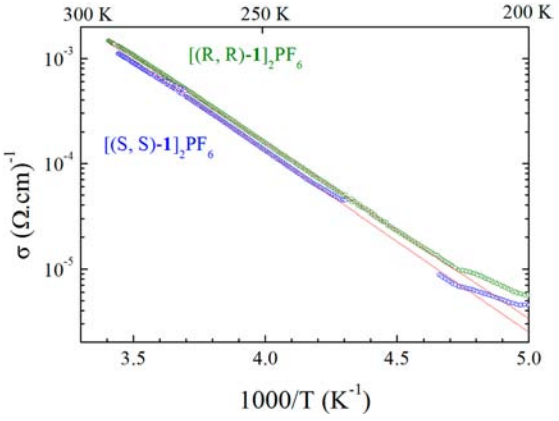

Figure 6. Temperature dependence of the electrical conductivity, σ, plotted as log σ versus the inverse temperature, for single crystals of $[(S,S)\text{-}\mathbf{1}]_2PF_6$ and $[(R,R)\text{-}\mathbf{1}]_2PF_6$ at ambient pressure. The red lines are the fit to the data giving an activation energy E_a = 3900 K.

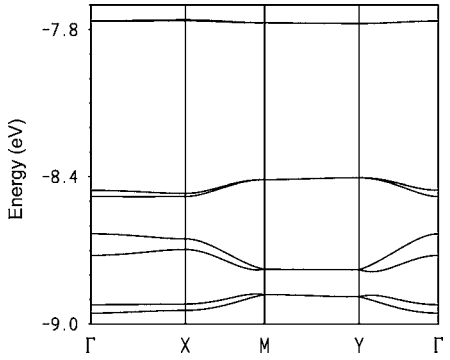

Figure 7. Calculated band structure for the donor layers of the $[(S,S)\text{-}\mathbf{1}]_2PF_6$ salt. Γ = (0, 0), X = (a*/2, 0), Y = (0, b*/2), and M = (a*/2, b*/2).

of the HOMO of donors **A** and **B**. In contrast, the filled bands have contributions of all donors HOMO although those of **C** and **D** have stronger weight. These results are easy to understand when the different $|\beta_{HOMO-HOMO}|$ interaction energies are considered. The calculated values (in eV) along the stacks are: 0.6999 (**A**−**B**), 0.3662 (**A**−**C**), 0.3416 (**B**−**D**), and 0.1143 (**C**−**D**). The interstack interactions are all quite small with only two exceptions, 0.0302 (**B**−**C**) and 0.0319 (**A**−**D**); they are all weaker than 0.0100. Many of the interstack interactions are not associated with short S···S contacts or in any case even if there have some, the energy difference between the different HOMOs makes the interaction very small. It is clear from these results that there is a strong interaction between donors **A** and **B** which leads to a strong dimerization, and thus the antibonding $HOMO_A-HOMO_B$ orbital is strongly pushed up and leads to the upper pair of bands. The bonding $HOMO_A-HOMO_B$ orbital is not that far in energy from the $HOMO_C$ and $HOMO_D$, and since the interaction energies **A**−**C** and **B**−**D** are still considerably strong, the bonding $HOMO_A-HOMO_B$, $HOMO_C$, and $HOMO_D$ interact. Unfortunately the interaction **C**−**D** is around six times smaller than **A**−**B** and three times smaller than **A**−**C** and **B**−**D** so that the HOMO···HOMO interaction along the stacks is severely cut at the **C**−**D** contact. This is why the lower filled bands exhibit some dispersion along the stacks direction, i.e., b, although not quite strong. As expected, the interstack dispersion is weak. In short, the strong dimerization of two of the donors imposes the activated conductivity of the (S,S) and (R,R) salts.

At ambient pressure, resistivity measurements on a single crystal of $[(rac)\text{-}\mathbf{1}]_2PF_6$ show a metallic behavior in the high-temperature range with a rather high-conductivity value of 250 $S{\cdot}cm^{-1}$ at room temperature (Figure 8). Then, a MI transition occurs at T_{MI} = 110 K (defined as the maximum of the derivative of log ρ versus $1/T$); the activation energy can be evaluated to E_a = 400 K around 50 K (Figure S6).

By applying hydrostatic pressure, the room-temperature conductivity increases linearly with a rate of 17%/kbar (Figure S7), and concomitantly, the MI transition is gradually shifted toward lower temperatures, i.e., $T_{MI} \approx$ 30 K at 8 kbar. Moreover, at 11.5 kbar the material remains metallic down to 50 mK (Figures 8 and S8), thus clearly indicating the suppression of the MI transition under pressure.

Band structure calculations have been performed on this $[(rac)\text{-}\mathbf{1}]_2PF_6$ salt starting from the single crystal X-ray structures at both room-temperature and 100 K, which is below the MI transition temperature observed in the conductivity curve. Note that from a crystallographic point of

dx.doi.org/10.1021/ja408350r | J. Am. Chem. Soc. 2013, 135, 17176−17186

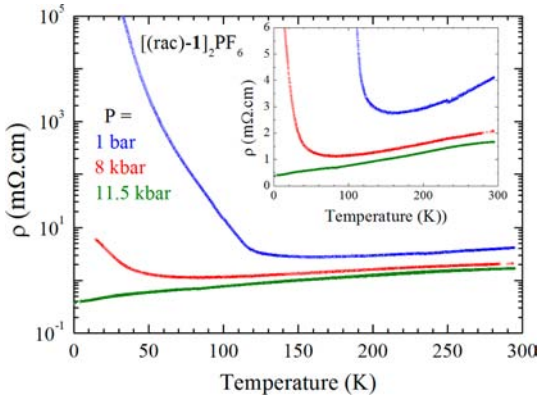

Figure 8. Temperature dependence of the electrical resistivity ρ for a single crystal of $[(rac)\text{-}\mathbf{1}]_2PF_6$ for three different pressures (1 bar and 8 and 11.5 kbar). The inset shows the same data with a linear scale for resistivity.

view the two structures are very similar (*vide supra*). The donor layers of the salt contain one symmetry nonequivalent donor and five different donor···donor interactions labeled I–V in Figure 9.

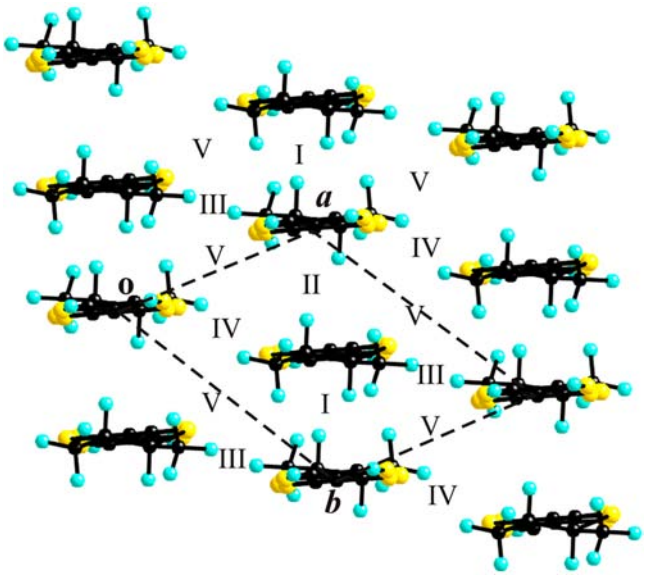

Figure 9. Donor layer of the $[(rac)\text{-}\mathbf{1}]_2PF_6$ salt where the five different intermolecular interactions are labeled.

The different S···S contacts shorter than 3.9 Å for every donor···donor interaction and the associated $|\beta_{HOMO-HOMO}|$ interaction energies for this salt are reported in Table 4.

Table 4. S···S Distances Shorter Than 3.9 Å and Absolute Values of the $|\beta_{HOMO-HOMO}|$ Interaction Energies (eV) for the Different Donor···Donor Interactions in the $[(rac)\text{-}\mathbf{1}]_2PF_6$ Salt at Room Temperature

interaction	S···S (<3.9 Å)	$\lvert\beta_{HOMO-HOMO}\rvert$ (eV)
I	3.665 (×2), 3.670 (×2)	0.7198
II	3.628 (×2)	0.6097
III	3.467 (×2), 3.782 (×2)	0.0400
IV	3.571 (×2), 3.798	0.0285
V	3.709, 3.781, 3.896	0.0692

The interactions along the stacks, although geometrically very different, are quite similar from the viewpoint of the HOMO···HOMO interactions. Thus, these stacks, running along the $(a-b)$ direction of the crystal structure, can be regarded as quite uniform chains of interacting HOMOs. Consequently, the two bands of the system should exhibit strong dispersion along this direction (not far from Γ→S in the reciprocal space)[24] and considerably smaller along the perpendicular direction (not far from Γ→M in the reciprocal space). The calculated band structure (Figure 10a) is in

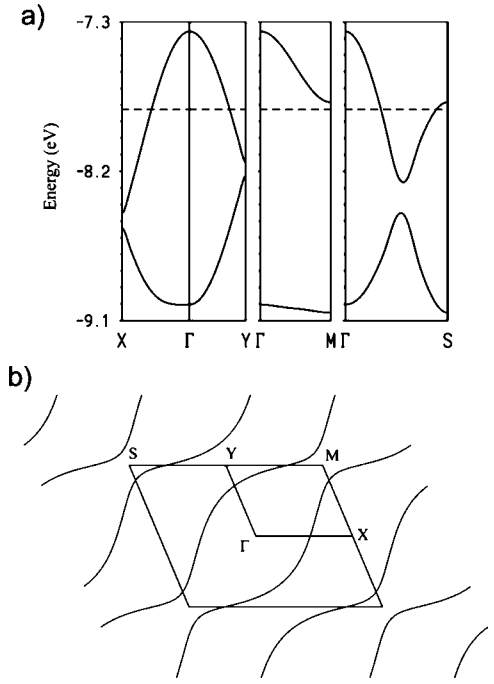

Figure 10. Calculated band structure (a) and Fermi surface (b) for the donor layers of the $[(rac)\text{-}\mathbf{1}]_2PF_6$ salt at room temperature. The dashed line in (a) refers to the Fermi level and Γ = (0, 0), X = ($a^*/2$, 0), Y = (0, $b^*/2$), M = ($a^*/2$, $b^*/2$), and S = ($-a^*/2$, $b^*/2$).

agreement with this analysis. In addition, the interstack interactions (III–V) are 1 order of magnitude smaller, but their contributions add to give a quite sizable dispersion to the upper band along the interstack direction (i.e., approximately along Γ→M) so that the system should be seen as a series of considerably coupled and quite uniform stacks along the $(a-b)$ direction.

This is confirmed by the calculated Fermi surface (Figure 10b) which is built from a series of warped open lines perpendicular to the stack direction. Thus, the present racemic salt is a pseudo-one-dimensional metal at room temperature. Note that the upper band at the M point is not far from the Fermi level. Consequently, relatively weak structural changes could close the Fermi surface lines which would then become elliptical in shape (i.e., a typical two-dimensional metal). This Fermi surface exhibits nesting vectors with an a^* component not far from 1/2. However, these vectors only lead to a partial nesting so that the Fermi surface could be only partially destroyed by modulations associated with such nesting vectors. Thus, typical charge or spin density modulations are unlikely to be at the origin of the quite abrupt MI transition of this material.

dx.doi.org/10.1021/ja408350r | J. Am. Chem. Soc. 2013, 135, 17176–17186

The calculations for the 100 K structure (Figure S10) are very similar to those for the room-temperature structure. The results are those one could expect by simply considering the thermal contraction associated with the transit from room temperature to 100 K (moderate shortening of S···S contacts and increase of the associated HOMO···HOMO interactions). Consequently these results are at odds with the observation of a quite abrupt MI transition at around 120−130 K at ambient pressure. As mentioned, a modulation either of the charge or spin type is unlikely to lead to such transition as there is no perfect nesting of the Fermi surface. Since the unit cell size does not change, the possibility of an electronic localization should be considered. In principle this kind of structural and electronic instability in quarter-filled metals can lead to two different "dimerizations", i.e., charge ordered state, with an alternation of charge-rich and -poor donors or Mott dimerization, with the hole located within a donor dyad, both molecules of donors being equally charged at +0.5 (Figure S11). The first situation would be accompanied by a symmetry lowering and, consequently, the existence of two independent donor molecules in the asymmetric unit bearing different positive charges. This would involve a charge differentiation of the two enantiomers. However, refinement of the 100 K structure in the noncentrosymmetric space group *P*1 did not allow any improvement when compared to the centrosymmetric *P*-1 structure, but on the contrary, the quality is much lower. Nevertheless, in order to gain more convincing proofs of the occurrence or not of charge ordering in the low temperature insulating state of $[(rac)\text{-}\mathbf{1}]_2PF_6$, single crystal Raman spectroscopy measurements have been performed on the whole family of compounds.

Single Crystal Raman Spectroscopy Study. It is known that the MI phase transition in the quarter-filled molecular conductors is often related to charge-ordering (CO) originating from Coulomb repulsion.[25] Vibrational spectroscopies, both Raman and infrared (IR) have been widely used in the characterization of CO states in BEDT-TTF-based salts.[25−27] Investigations of vibrational structure are usually focused on the C═C stretching modes that display large frequency shift due to oxidation. In particular, the Raman-active ν_2 mode that is assigned to totally symmetric ring C═C stretching and the IR-active ν_{27} mode attributed to out-of-phase ring C═C stretching are characterized by the linear relationship between the frequency and the charge on the molecule.[27a] In order to estimate the charge localized on the donor molecules in the $(\mathbf{1})_2PF_6$ family of materials, theoretical calculations of vibrational modes for both the neutral **1** and radical cation $\mathbf{1}^{+\bullet}$ have been performed, by focusing on the C═C stretching modes useful for the charge estimation. Three modes are found, schematically shown in Figure 11. Here, the ν_A mode shows similar displacements to the ν_2 mode of the BEDT-TTF molecule, ν_B is similar to ν_{27}, and the ν_C mode is the counterpart of ν_3 in BEDT-TTF. While all the three modes are Raman-active, the ν_B mode displays the strongest frequency dependence on the charge.

Figure 12a shows the experimental Raman spectrum of the neutral **1** at room temperature in the frequency range of the C═C stretching modes together with its theoretical spectrum. The calculated frequencies and also relative intensities of the three fundamental C═C stretching vibrations are in agreement with the experimental frequencies. Accordingly, the assignments for the three modes are as follows: the one centered at 1559 cm^{-1} in the experimental spectrum as ν_A found in the theoretical spectrum at 1580 cm^{-1}, the one at 1527 cm^{-1} (experimental) as ν_B (theoretical, 1543 cm^{-1}), and the one at 1509 cm^{-1} (experimental) as ν_C (theoretical, 1523 cm^{-1}). Based on DFT calculations all the three C═C stretching modes of interest here display significant frequency shift due to oxidation of the donor molecule. The ν_A mode shifts by 65 cm^{-1} to 1515 cm^{-1} in $\mathbf{1}^{+\bullet}$, the ν_B mode shifts by 140 cm^{-1} to 1403 cm^{-1}, and the ν_C mode shifts by 80 cm^{-1} to 1443 cm^{-1}. Thus the most charge sensitive is the ν_B mode, and this result is reminiscent of the strong frequency dependence on charge in the case of ν_{27} in BEDT-TTF.[27] To describe the relationship between the frequency and charge for **1** in a more quantitative manner, room-temperature Raman spectra of a 1:1 radical cation salt of **1** with the triiodide anion, namely $[(S,S)\text{-}\mathbf{1}](I_3)$, have been measured (Figure 12b). For this salt the charge on the donor molecules is +1. Here, four vibrational features are found, compared with the three theoretical C═C modes. Taking into account similar frequencies, the 1501 cm^{-1} mode in the experimental spectrum is assigned as ν_A, the one centered at 1438 cm^{-1} as ν_C, and the mode at 1407 cm^{-1} as the most charge sensitive ν_B. The origin of the mode centered at 1476 cm^{-1} in the spectrum of $[(S,S)\text{-}\mathbf{1}](I_3)$ is not known yet, but its position suggests a relation with the ν_B and ν_C modes of **1** charged +0.5. Based on these findings, the relationship between the frequency and the charge ρ on the DM-EDT-TTF molecule **1** for the ν_B mode is $\nu_B(\rho) = 1407 + 120(1 - \rho)$ cm^{-1}.

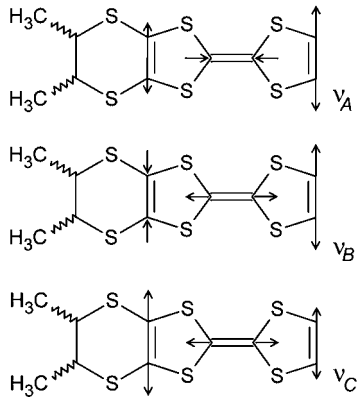

Figure 11. Three fundamental charge sensitive C═C stretching modes of the DM-EDT-TTF molecule **1**.

In order to check the possibility of low-temperature charge localization in $[(rac)\text{-}\mathbf{1}]_2PF_6$, single crystal Raman spectra of the three members of the $(\mathbf{1})_2PF_6$ family of salts have been investigated in the temperature range 10−300 K. While both $[(S,S)\text{-}\mathbf{1}]_2PF_6$ and $[(R,R)\text{-}\mathbf{1}]_2PF_6$ materials display similar features with no significant temperature dependence, the racemic material shows different Raman spectra. However, once again, no temperature dependence was found for this salt (Figure 13a) in spite of the quite abrupt MI phase transition at about 120 K in the resistivity curve. The spectra measured at 10 K for all materials are compared in Figure 13b, together with the experimental spectrum of $[(S,S)\text{-}\mathbf{1}](I_3)$.

The single crystal Raman analysis in the case of the enantiopure $(\mathbf{1})_2PF_6$ salts is in agreement with the structural analysis showing the existence of four independent donors **A**−**D** in the unit cell (*vide supra*), as the Raman spectra of these semiconducting materials (Figure 13b) indicate that there are sets of differently charged donor molecules in the structure. The modes at 1399, 1450, and 1500 cm^{-1} are assigned as ν_B, ν_C, and ν_A, respectively, of $\mathbf{1}^{+\bullet}$. A weak shoulder that appears at

dx.doi.org/10.1021/ja408350r | J. Am. Chem. Soc. 2013, 135, 17176−17186

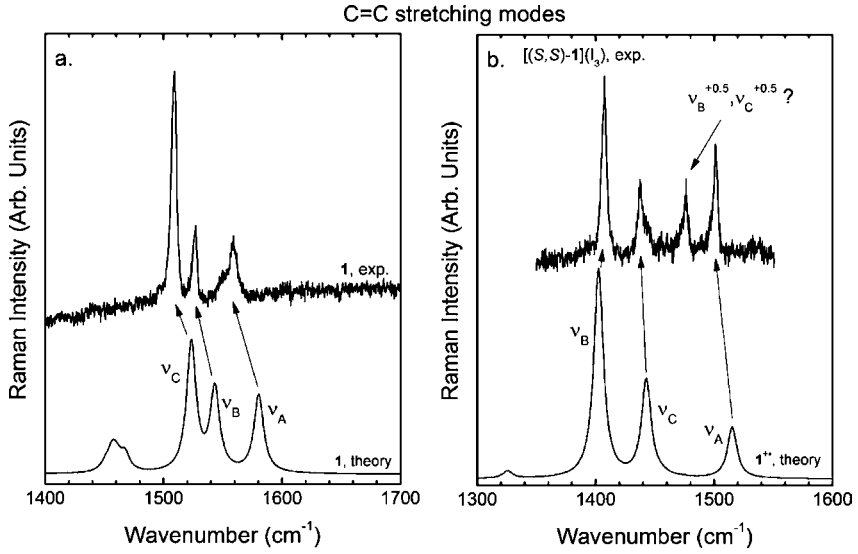

Figure 12. Experimental Raman spectra, measured with the 632.8 nm excitation line, of neutral DM-EDT-TTF **1** (a) and [(*S*,*S*)-**1**](I$_3$) (b) single crystals in the frequency range of the C=C stretching modes, together with the respective theoretical Raman spectra of **1** and **1**$^{+\bullet}$ calculated at the B3LYP/LanL2DZ level of theory. Note that the spectra in both panels are offset for clarity.

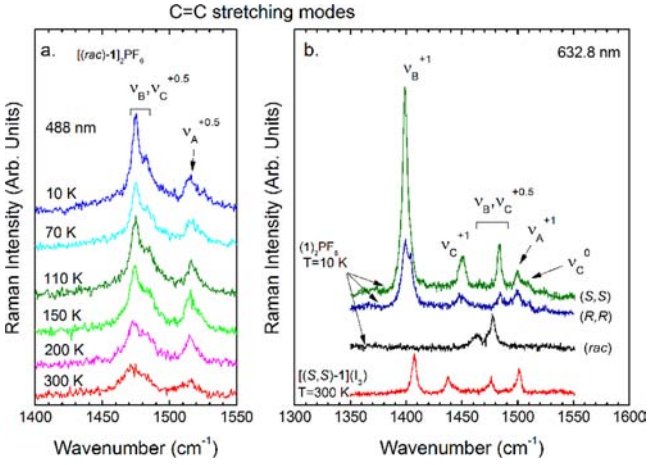

Figure 13. Raman spectra in the frequency range of the C=C stretching modes of [(*rac*)-**1**]$_2$PF$_6$ measured for the excitation line at 488 nm (a), and the whole series of (**1**)$_2$PF$_6$ salts, together with [(*S*,*S*)-**1**](I$_3$) for comparison, measured for the excitation line at 632.8 nm (b). Note that the spectra in both panels are offset for clarity.

about 1509 cm^{-1} is attributed to the ν_C mode of neutral **1**. Another mode at 1484 cm^{-1} is most probably related to ν_B and/or ν_C of **1**$^{+0.5}$. This suggests that DM-EDT-TTF donor molecules with the charges 0, +0.5, and +1 are present in the structure within the time scale of the Raman measurements.

On the other hand, the Raman spectra of [(*rac*)-**1**]$_2$PF$_6$ in the frequency range of the C=C stretching modes basically display two slightly broadened bands at 1463 and 1478 cm^{-1} that differ in shape and frequency between measurements performed using different laser excitation lines (compare Figures 13a and 13b). This doublet structure can be very likely related to ν_B and ν_C of **1**$^{+0.5}$. Another mode at about 1516 cm^{-1} that is found in the spectra measured using 514.5 nm (not shown) and 488 nm (Figure 13a) excitation lines is attributed to ν_A of **1**$^{+0.5}$. These results are in agreement with the crystal structure showing only one nonequivalent donor molecule in the unit cell, with the average charge of +0.5. The observed broadening of the 1463/1478 cm^{-1} doublet structure could be related to some charge fluctuations.[28] No splitting of either of these modes is observed down to 10 K, which provides solid evidence that the MI transition observed in the resistivity curve is not related to a charge ordering in the material. Therefore, the most likely explanation for MI transition is the occurrence of a Mott "dimerization" type ordering.

CONCLUSIONS

The enantiopure methylated donors (*S*,*S*) and (*R*,*R*)-DM-EDT-TTF have been synthesized and structurally characterized. The first crystalline radical cation salts based on these chiral donors are prepared by the electrocrystallization technique leading to the series of mixed valence salts [(*S*,*S*)-**1**]$_2$PF$_6$, [(*R*,*R*)-**1**]$_2$PF$_6$, and [(*rac*)-**1**]$_2$PF$_6$ structurally characterized. While four independent donor molecules bearing different positive charges between 0 and +1 are present in the enantiopure salts, the racemic compound shows only one nonequivalent donor in the mixed valence state +0.5. Single crystal conductivity measurements supported by tight-binding band structure calculations clearly indicate semiconducting behavior for the enantiopure materials, while the racemic one is metallic down to 120 K at ambient pressure. An applied isotropic pressure of 11.5 kbar allows the suppression of the MI transition, which is very likely of Mott-type localization according to temperature-dependent single crystal Raman spectroscopy measurements. The crucial role of the chiral information is thus evidenced in this family of crystalline conducting salts. To the best of our knowledge, this is the first case when the racemic salt is more conducting than the enantiopure counterparts. These results open the way toward the preparation of new radical cation salts based on the DM-EDT-TTF donor as a step further in the search of chiral conductors showing synergy between chirality and electrical conductivity.

EXPERIMENTAL SECTION

Materials and Instrumentation. Reactions were carried out under argon, dry solvents were obtained from solvent drying machines. Nuclear magnetic resonance spectra were

Table 5. Crystallographic Data, Details of Data Collection, and Structure Refinement Parameters for the Neutral Donors and Their Radical Cation Salts

	(*S*,*S*)-**1**	(*R*,*R*)-**1**	$[(S,S)\text{-}\mathbf{1}]_2PF_6$	$[(R,R)\text{-}\mathbf{1}]_2PF_6$	$[(rac)\text{-}\mathbf{1}]_2PF_6$	$[(rac)\text{-}\mathbf{1}]_2PF_6$ 100 K
formula	$C_{10}H_{10}S_6$	$C_{10}H_{10}S_6$	$C_{20}H_{20}F_6PS_{12}$	$C_{20}H_{20}F_6PS_{12}$	$C_{20}H_{20}F_6PS_{12}$	$C_{20}H_{20}F_6PS_{12}$
M [g mol^{-1}]	322.54	322.54	790.05	790.05	790.05	790.05
T [K]	293(2)	293(2)	293(2)	293(2)	293(2)	100(2)
crystal system	orthorhombic	orthorhombic	monoclinic	monoclinic	triclinic	triclinic
space group	$P2_12_12_1$	$P2_12_12_1$	$P2_1$	$P2_1$	$P\text{-}1$	$P\text{-}1$
a [Å]	9.1424(6)	9.1575(13)	13.1473(12)	13.1431(16)	6.6660(4)	6.5771(5)
b [Å]	11.0497(5)	11.0492(11)	15.675(3)	15.707(2)	8.3842(8)	8.3478(10)
c [Å]	13.7839(11)	13.757(2)	15.485(2)	15.474(3)	15.2213(19)	15.004(3)
α [°]	90.00	90.00	90.00	90.00	86.281(8)	83.296(13)
β [°]	90.00	90.00	107.286(10)	107.326(14)	77.464(7)	77.863(11)
γ [°]	90.00	90.00	90.00	90.00	67.141(6)	67.014(10)
V [Å^3]	1392.46(16)	1392.0(3)	3047.0(7)	3049.6(9)	765.03(13)	740.86(17)
Z	4	4	4	4	1	1
ρ_{calcd} [g cm^{-3}]	1.539	1.539	1.722	1.721	1.715	1.771
μ [mm^{-1}]	0.952	0.952	0.964	0.963	0.960	0.991
goodness-of-fit on F^2	1.214	1.064	1.027	1.047	1.039	1.046
final $R1/wR2$ [$I > 2\sigma(I)$]	0.0508/0.0880	0.0765/0.1879	0.0549/0.1188	0.0491/0.1173	0.0540/0.1112	0.0505/0.1096
$R1/wR2$ (all data)	0.0795/0.1027	0.1175/0.2136	0.1073/0.1451	0.0844/0.1385	0.1037/0.1318	0.0802/0.1236

recorded on a Bruker Avance DRX 300 spectrometer operating at 300 MHz for ^{1}H and 75 MHz for ^{13}C. Chemical shifts are expressed in parts per million (ppm) downfield from external TMS. The following abbreviations are used: s, singlet; d, doublet; dq, doublet of quadruplets; m, multiplet. MALDI-TOF MS spectra were recorded on Bruker Biflex-IIITM apparatus, equipped with a 337 nm N_2 laser. Elemental analyses were recorded using Flash 2000 Fisher Scientific Thermo Electron analyzer.

Syntheses. *(S,S)-(4,5-Bis(methoxycarbonyl)-1,3-dithiol-2-ylidene)-5,6-dihydro-5,6-dimethyl-1,3-dithiolo[4,5-b][1,4]-dithiin [(S,S)-**4**].* (*S*,*S*)-**2** (2.5 g, 10 mmol) and dimethyl 2-oxo-1,3-dithiole-4,5-dicarboxylate **3** (4.68 g, 20 mmol, 2 equiv) were mixed under argon in 30 mL of freshly distilled trimethylphosphite, and the mixture was heated at 110 °C for 5 h. The solvent was evaporated in a rotary evaporator, and then 40 mL of toluene was added and evaporated. The last procedure was repeated twice. The product was solubilized in dichloromethane and passed down a silica column to remove the remaining phosphate and then purified by chromatography using petroleum spirit/dichloromethane 1/1 to afford a red-brown solid (1.6 g, 37%). Red-brown single crystals were obtained by slow evaporation of a diethylether solution. ^{1}H NMR (300 MHz, $CDCl_3$): δ 3.83 (s, 6H, $-OCH_3$), 3.29 (m, 2H, 4-, 5-SC*H*), 1.43 (d, 6H, J = 6.6 Hz, $-CH_3$) ppm; ^{13}C NMR (75 MHz, $CDCl_3$): δ 159.8 (CO_2Me), 131.9 (CCO_2Me), 112.2, 110.7, 110.4, 53.3 ($COOCH_3$), 44.3 (*C*H-Me), 21.7 ($CHCH_3$) ppm; MS (MALDI-TOF) m/z: 437.4 (M_{th} = 437.92).

*(R,R)-(4,5-Bis(methoxycarbonyl)-1,3-dithiol-2-ylidene)-5,6-dihydro-5,6-dimethyl-1,3-dithiolo[4,5-b][1,4]dithiin [(R,R)-**4**].* The same synthetic procedure was followed as for the (*S*,*S*) enantiomer starting from (*R*,*R*)-**2**. Yield 37%.

*(S,S)-DMEDT-TTF [(S,S)-**1**].* (*S*,*S*)-**4** (0.66 g, 1.5 mmol) and LiBr (2.34 g, 27 mmol, 18 equiv) were mixed in 60 mL of dimethylformamide. The solution was stirred at 150 °C for 30 min, the formation of the product being monitored by TLC. The product was extracted with dichloromethane, and the organic phase was washed with brine and water and then dried over $MgSO_4$. The solvent was removed under vacuum, and the product was purified by chromatography on a silica column with petroleum spirit/dichloromethane 1/1 to afford a yellow orange solid (0.24 g, 40%). ^{1}H NMR (300 MHz, $CDCl_3$): δ 6.32 (s, 2H, $-SCH=$), 3.19 (m, 2H, 4-, 5-SC*H*), 1.42 (d, 6H, J = 5.7 Hz, $-CH_3$) ppm; ^{13}C NMR (75 MHz, $CDCl_3$): δ 118.9 ($-SCH=$), 118.0, 104.3, 44.3 (*C*H-Me), 21.7 ($CHCH_3$) ppm; MS (MALDI-TOF) m/z: 321.9 (M_{th} = 321.91); Elemental analysis calcd. (%) for $C_{10}H_{10}S_6$: C 37.23, H 3.12, S 59.64; found: C 37.35, H 3.05, S 59.00.

*(R,R)-DMEDT-TTF [(R,R)-**1**].* The same synthetic procedure was followed as for the (*S*,*S*)-**1** enantiomer starting from (*R*,*R*)-**4**. Yield 37%. MS (MALDI-TOF) m/z: 321.9 (M_{th} = 321.91); Elemental analysis calcd. (%) for $C_{10}H_{10}S_6$: C 37.23, H 3.12, S 59.64; found: C 37.44, H 3.06, S 59.81.

$[(S,S)\text{-}\mathbf{1}]_2PF_6$. Twelve mg of $[NBu_4]PF_6$ was dissolved in 6 mL $CHCl_3$, and the solution was poured into the cathodic compartment of the electrocrystallization cell. The anodic chamber was filled with 5 mg of $[(S,S)\text{-}\mathbf{1}]$ dissolved in 6 mL $CHCl_3$. Single crystals of the salt were grown at 20 °C over a period of 2 weeks on a platinum wire electrode, by applying a constant current of 0.5 μA. Solid black plates were collected on the electrode.

$[(R,R)\text{-}\mathbf{1}]_2PF_6$. Same conditions and amounts as previously described were employed.

$[(rac)\text{-}\mathbf{1}]_2PF_6$. Twelve mg of $[NBu_4]PF_6$ was dissolved in 6 mL $CHCl_3$, and the solution was poured into the cathodic compartment of the electrocrystallization cell. The anodic chamber was filled with 5 mg of (*rac*)-**1**, prepared from 2.5 mg $[(S,S)\text{-}\mathbf{1}]$ and 2.5 mg $[(R,R)\text{-}\mathbf{1}]$ dissolved in 6 mL $CHCl_3$. Single crystals of the salt, as thin brown plates, were grown in solution at 20 °C over a period of 10 days, by applying a constant current of 0.5 μA on a platinum wire electrode.

Enantioenriched Mixture of 1. Twelve mg of $[NBu_4]PF_6$ was dissolved in 6 mL $CHCl_3$, and the solution was poured into the cathodic compartment of the electrocrystallization cell. The anodic chamber was filled with 1.25 mg of (*R*,*R*)-**1** and 3.75 mg of (*S*,*S*)-**1**) (50% ee of (*S*,*S*)-**1**) dissolved in 6 mL $CHCl_3$. Two types of crystals were clearly formed. Single crystals of the enantiopure $[(S,S)\text{-}\mathbf{1}]_2PF_6$ salt were grown at 20 °C over a period of 7 days on the platinum wire electrode, by applying a

dx.doi.org/10.1021/ja408350r | J. Am. Chem. Soc. 2013, 135, 17176−17186

constant current of 0.5 μA, while crystals of the racemic [(*rac*)-**1**]$_2$PF$_6$ salt were collected from the bottom of the cell.

Crystallography. X-ray diffraction measurements were performed on a Nonius Kappa CCD diffractometer, using graphite-monochromated MoK_α radiation (λ = 0.71073 Å). The structures were solved (SHELXS-97) by direct methods and refined (SHELXL-97) by full-matrix least-squares procedures on F^2.[29] The non-H atoms were refined with anisotropic displacement parameters. A summary of the crystallographic data and the structure refinement is given in Table 5. CCDC reference numbers: CCDC 955148 (*S*,*S*)-**1**, CCDC 955149 (*R*,*R*)-**1**, CCDC 955150 [(*S*,*S*)-**1**]$_2$PF$_6$, CCDC 955151 [(*R*,*R*)-**1**]$_2$PF$_6$, CCDC 955152 [(*rac*)-**1**]$_2$PF$_6$, and CCDC 955153 [(*rac*)-**1**]$_2$PF$_6$ at 100 K. These data can be obtained free of charge from The Cambridge Crystallographic Data Centre via www.ccdc.cam.ac.uk/data_request/cif.

Single Crystal Conductivity Measurements. Electrical resistivity was measured on platelet-shaped single crystals using a four point method. Four gold contacts were evaporated on both faces of the crystals, and gold wires were glued with silver paste on those contacts. A low-frequency (<100 Hz) lock-in technique with a measuring current I_{ac} = 1 μA was used for resistance values lower than 50 kΩ, while higher resistances were measured with dc currents ranging from 100 to 0.5 nA. Resistivity measurements were also performed under high hydrostatic pressure in a CuBe clamped cell up to 12 kbar with silicon oil (Daphne 7373) as the pressure transmitting medium. The pressure at room temperature was extracted from the resistance of a manganin gauge in the pressure cell, and it is this value that is indicated in the figures. However, the loss of pressure during cooling is estimated to 2 kbar. A copper-constantan thermocouple inside the pressure cell was used as the thermometer. Resistivity measurements were performed in the range 15−300 K using a cryocooler equipment except for the highest pressure experiment which has been performed in a dilution refrigerator down to 50 mK.

Band Structure Calculations. The tight-binding band structure calculations were of the extended Hückel type.[30] A modified Wolfsberg−Helmholtz formula was used to calculate the nondiagonal $H_{\mu\nu}$ values.[31] All valence electrons were taken into account in the calculations, and the basis set consisted of Slater-type orbitals of double-ζ quality for C 2s and 2p, S 3s and 3p, and of single-ζ quality for H. The ionization potentials, contraction coefficients, and exponents were taken from previous work.[32]

Single Crystal Raman Spectroscopy. Typical dimensions of single crystalline samples used in measurements were 0.4 × 0.1 × 0.1 mm^3 ([(*rac*)-**1**]$_2$PF$_6$) and 0.3 × 0.2 × 0.1 mm^3 (([(*R*,*R*)-**1**]$_2$PF$_6$ and [(*S*,*S*)-**1**]$_2$PF$_6$). The optical axes of the crystals were determined as those displaying the largest anisotropy at 300 K. Raman spectra for the electrical vector of the laser beam parallel to the direction of the maximum C=C stretching band intensity were measured in a backward scattering geometry with a Raman LABRAM HR800 spectrometer equipped with a microscope. He−Ne (λ = 632.8 nm) and Ar (λ = 514.5, 488 nm) laser lines were used with power reduced to about 0.1 mW to avoid sample overheating. The spectra were recorded with spectral resolution of 2 cm^{-1} at several temperatures between 10 and 300 K, and the temperature was controlled with an Oxford Instruments continuous-flow cryostat. Room-temperature Raman spectra of reference materials, neutral DM-EDT-TTF **1** (polycrystalline sample) and [(*S*,*S*)-**1**](I$_3$) salt (single crystals) were also measured.

■ ASSOCIATED CONTENT

Supporting Information

Full experimental section including description of the synthesis and characterization of all new materials and all the techniques employed in the research reported here. This information is available free of charge via the Internet at http://pubs.acs.org.

■ AUTHOR INFORMATION

Corresponding Author

narcis.avarvari@univ-angers.fr

Notes

The authors declare no competing financial interest.

■ ACKNOWLEDGMENTS

This work was supported in France by the National Agency for Research (ANR, Project 09-BLAN-0045-01), the CNRS and the University of Angers. Financial support from the COST Action D35 is also gratefully acknowledged. Work at Bellaterra (Spain) was supported by the Spanish Ministerio de Economía y Competitividad (grants FIS2012-37549-C05-05 and CSD2007-00041). Work at Poznan (Poland) was supported by the National Science Centre (decision no. DEC-2012/04/M/ST3/00774).

■ REFERENCES

(1) Avarvari, N.; Wallis, J. D. *J. Mater. Chem.* **2009**, *19*, 4061−4076.

(2) (a) Coronado, E.; Day, P. *Chem. Rev.* **2004**, *104*, 5419−5448. (b) Coronado, E.; Galán-Mascarós, J. R. *J. Mater. Chem.* **2005**, *15*, 66−74.

(3) Dunitz, J. D.; Karrer, A.; Wallis, J. D. *Helv. Chim. Acta* **1986**, *69*, 69−70.

(4) Hasegawa, M.; Sone, Y.; Iwata, S.; Matsuzawa, H.; Mazaki, Y. *Org. Lett.* **2011**, *13*, 4688−4691.

(5) Krstić, V.; Roth, S.; Burghard, M.; Kern, K.; Rikken, G. L. J. A. *J. Chem. Phys.* **2002**, *117*, 11315−11319.

(6) (a) Réthoré, C.; Fourmigué, M.; Avarvari, N. *Chem. Commun.* **2004**, 1384−1385. (b) Réthoré, C.; Avarvari, N.; Canadell, E.; Auban-Senzier, P.; Fourmigué, M. *J. Am. Chem. Soc.* **2005**, *127*, 5748−5749. (c) Madalan, A. M.; Réthoré, C.; Fourmigué, M.; Canadell, E.; Lopes, E. B.; Almeida, M.; Auban-Senzier, P.; Avarvari, N. *Chem.—Eur. J.* **2010**, *16*, 528−537.

(7) (a) Riobé, F.; Avarvari, N. *Chem. Commun.* **2009**, 3753−3755. (b) Riobé, F.; Avarvari, N. *Coord. Chem. Rev.* **2010**, *254*, 1523−1533.

(8) Yang, S.; Brooks, A. C.; Martin, L.; Day, P.; Li, H.; Horton, P.; Male, L.; Wallis, J. D. *CrystEngComm* **2009**, *11*, 993−996.

(9) (a) Danila, I.; Riobé, F.; Piron, F.; Puigmartí-Luis, J.; Wallis, J. D.; Linares, M.; Ågren, H.; Beljonne, D.; Amabilino, D. B.; Avarvari, N. *J. Am. Chem. Soc.* **2011**, *133*, 8344−8353. (b) Danila, I.; Pop, F.; Escudero, C.; Feldborg, L. N.; Puigmartí-Luis, J.; Riobé, F.; Avarvari, N.; Amabilino, D. B. *Chem. Commun.* **2012**, *48*, 4552−4554.

(10) Chas, M.; Lemarié, M.; Gulea, M.; Avarvari, N. *Chem. Commun.* **2008**, 220−222.

(11) (a) Gómez, R.; Segura, J. L.; Martin, N. *J. Org. Chem.* **2000**, *65*, 7566−7574. (b) Zhou, Y.; Zhang, D.; Zhu, L.; Shuai, Z.; Zhu, D. *J. Org. Chem.* **2006**, *71*, 2123−2130. (c) Saad, A.; Barrière, F.; Levillain, E.; Vanthuyne, N.; Jeannin, O.; Fourmigué, M. *Chem.—Eur. J.* **2010**, *16*, 8020−8028. (d) Saad, A.; Jeannin, O.; Fourmigué, M. *Tetrahedron* **2011**, *67*, 3820−3829.

(12) Matsumiya, S.; Izuoka, A.; Sugawara, T.i; Taruishi, T.; Kawada, Y. *Bull. Chem. Soc. Jpn.* **1993**, *66*, 513−522.

(13) Zambounis, J. S.; Mayer, C. W. *Tetrahedron Lett.* **1991**, *32*, 2737−2740.

(14) Papavassiliou, G. C.; Zambounis, J. S.; Mousdis, G. A.; Gionis, V.; Yiannopoulos, S. Y. *Mol. Cryst. Liq. Cryst.* **1988**, *156*, 269−276.
(15) Pop, F.; Laroussi, S.; Cauchy, T.; Gómez-García, C. J.; Wallis, J. D.; Avarvari, N. *Chirality* **2013**, *25*, 466−474.
(16) Karrer, A.; Wallis, J. D.; Dunitz, J. D.; Hilti, B.; Mayer, C. W.; Bürkle, M.; Pfeiffer, J. *Helv. Chim. Acta* **1987**, *70*, 942−953.
(17) (a) Zambounis, J. S.; Mayer, C. W.; Hauenstein, K.; Hilti, B.; Hofherr, W.; Pfeiffer, J.; Bürkle, M.; Rihs, G. *Adv. Mater.* **1992**, *4*, 33−35. (b) Matsumiya, S.; Izuoka, A.; Sugawara, T.; Taruishi, T.; Kawada, Y.; Tokumoto, M. *Bull. Chem. Soc. Jpn.* **1993**, *66*, 1949−1954. (c) Krivickas, S. J.; Ichikawa, A.; Takahashi, K.; Tajima, H.; Wallis, J. D.; Mori, H. *Synth. Met.* **2011**, *161*, 1563−1565.
(18) Galán-Mascarós, J. R.; Coronado, E.; Goddard, P. A.; Singleton, J.; Coldea, A. I.; Wallis, J. D.; Coles, S. J.; Alberola, A. *J. Am. Chem. Soc.* **2010**, *132*, 9271−9273.
(19) Terzis, A.; Hountas, A.; Underhill, A. E.; Clark, A.; Kaye, B.; Hilti, B.; Mayer, C.; Pfeiffer, J.; Yiannopoulos, S. Y.; Mousdis, G.; Papavassiliou, G. C. *Synth. Met.* **1988**, *27*, B97−B102.
(20) Garreau, B.; de Montauzon, D.; Cassoux, P.; Legros, J.-P.; Fabre, J.-M.; Saoud, K.; Chakroune, S. *New J. Chem.* **1995**, *19*, 161−171.
(21) Liu, W.; Guenet, J.-M.; Green, M. M. *Chirality* **2004**, *16*, 661−664.
(22) Mori, T. *Bull. Chem. Soc. Jpn.* **1998**, *71*, 2509−2526.
(23) Martin, L.; Day, P.; Akutsu, H.; Yamada, J.; Nakatsuji, S.; Clegg, W.; Harrington, R. W.; Horton, P. N.; Hursthouse, M. B.; McMillan, P.; Firth, S. *CrystEngComm.* **2007**, *9*, 865−867.
(24) The G→S line crosses the border of the Wigner−Seitz Brillouin zone, and this is why around the center of the line the bands change slope. Only the first part until the change of slope must be considered to describe the interactions along the stacks.
(25) (a) Yamamoto, K.; Yakushi, K.; Miyagawa, K.; Kanoda, K.; Kawamoto, A. *Phys. Rev. B* **2002**, *65*, 0851110−1−0851110−8. (b) Yamamoto, K.; Uruichi, M.; Yakushi, K.; Yamaura, J.; Tajima, H. *Phys. Rev. B* **2004**, *70*, 125102−1−125102−11.
(26) Yue, Y.; Yamamoto, K.; Uruichi, M.; Nakano, C.; Yakushi, K.; Yamada, S.; Hiejima, T.; Kawamoto, A. *Phys. Rev. B* **2010**, *82*, 075134−1−075134−8.
(27) (a) Yamamoto, T.; Uruichi, M.; Yamamoto, K.; Yakushi, K.; Kawamoto, A.; Tanigushi, H. *J. Phys. Chem. B* **2005**, *109*, 15226−15235. (b) Girlando, A. *J. Phys. Chem. C* **2011**, *115*, 19371−19378.
(28) Girlando, A.; Masino, M.; Kaiser, S.; Sun, Y.; Drichko, N.; Dressel, M.; Mori, H. *Phys. Status Solidi B* **2012**, *5*, 953−956.
(29) Sheldrick, G. M. *Programs for the Refinement of Crystal Structures*; University of Göttingen: Göttingen, Germany, 1996.
(30) Whangbo, M.-H.; Hoffmann, R. *J. Am. Chem. Soc.* **1978**, *100*, 6093−6098.
(31) Ammeter, J. H.; Bürgi, H.-B.; Thibeault, J.; Hoffmann, R. *J. Am. Chem. Soc.* **1978**, *100*, 3686−3692.
(32) Pénicaud, A.; Boubekeur, K.; Batail, P.; Canadell, E.; Auban-Senzier, P.; Jérome, D. *J. Am. Chem. Soc.* **1993**, *115*, 4101−4112.